Biomedical Optics EXPRESS

Portable, parallel 9-wavelength near-infrared spectral tomography (NIRST) system for efficient characterization of breast cancer within the clinical oncology infusion suite

Yan Zhao,[1] Brian W. Pogue,[1] Steffen J. Haider,[1] Jiang Gui,[2] Roberta M. diFlorio-Alexander,[3] Keith D. Paulsen,[1] and Shudong Jiang[1,*]

[1]*Thayer School of Engineering, Dartmouth College, Hanover, NH 03755, USA*
[2]*Department of Radiology, Dartmouth Hitchcock Medical Center, Lebanon, NH 03756, USA*
[3]*Department of Community and Family Medicine, Geisel School of Medicine, Dartmouth College, Hanover, NH 03755, USA*
[*]*shudong.jiang@dartmouth.edu*

Abstract: A portable near-infrared spectral tomography (NIRST) system was developed with simultaneous frequency domain (FD) and continuous-wave (CW) optical measurements for efficient characterization of breast cancer in a clinical oncology setting. Simultaneous FD and CW recordings were implemented to speed up acquisition to 3 minutes for all 9 wavelengths, spanning a range from 661nm to 1064nm. An adjustable interface was designed to fit various breast sizes and shapes. Spatial images of oxy- and deoxy-hemoglobin, water, lipid, and scattering components were reconstructed using a 2D FEM approach. The system was tested on a group of 10 normal subjects, who were examined bilaterally and the recovered optical images were compared to radiographic breast density. Significantly higher total hemoglobin and water were estimated in the high density relative to low density groups. One patient with invasive ductal carcinoma was also examined and the cancer region was characterized as having a contrast ratio of 1.4 in total hemoglobin and 1.2 in water.

OCIS codes: (170.0110) Imaging systems; (170.6960) Tomography; (120.3890) Medical optics instrumentation; (170.6510) Spectroscopy, tissue diagnostics.

References and links

1. B. Fisher, A. Brown, E. Mamounas, S. Wieand, A. Robidoux, R. G. Margolese, A. B. Cruz, Jr., E. R. Fisher, D. L. Wickerham, N. Wolmark, A. DeCillis, J. L. Hoehn, A. W. Lees, and N. V. Dimitrov, "Effect of preoperative chemotherapy on local-regional disease in women with operable breast cancer: findings from National Surgical Adjuvant Breast and Bowel Project B-18," J. Clin. Oncol. **15**(7), 2483–2493 (1997).
2. A. B. Chagpar, L. P. Middleton, A. A. Sahin, P. Dempsey, A. U. Buzdar, A. N. Mirza, F. C. Ames, G. V. Babiera, B. W. Feig, K. K. Hunt, H. M. Kuerer, F. Meric-Bernstam, M. I. Ross, and S. E. Singletary, "Accuracy of physical examination, ultrasonography, and mammography in predicting residual pathologic tumor size in patients treated with neoadjuvant chemotherapy," Ann. Surg. **243**(2), 257–264 (2006).
3. C. E. Loo, M. E. Straver, S. Rodenhuis, S. H. Muller, J. Wesseling, M. J. Vrancken Peeters, and K. G. Gilhuijs, "Magnetic resonance imaging response monitoring of breast cancer during neoadjuvant chemotherapy: relevance of breast cancer subtype," J. Clin. Oncol. **29**(6), 660–666 (2011).
4. B. T. Miller, A. M. Abbott, and T. M. Tuttle, "The influence of preoperative MRI on breast cancer treatment," Ann. Surg. Oncol. **19**(2), 536–540 (2012).
5. D. Groheux, S. Giacchetti, M. Espié, D. Rubello, J. L. Moretti, and E. Hindié, "Early monitoring of response to neoadjuvant chemotherapy in breast cancer with 18F-FDG PET/CT: defining a clinical aim," Eur. J. Nucl. Med. Mol. Imaging **38**(3), 419–425 (2011).
6. A. Cerussi, N. Shah, D. Hsiang, A. Durkin, J. Butler, and B. J. Tromberg, "In vivo absorption, scattering, and physiologic properties of 58 malignant breast tumors determined by broadband diffuse optical spectroscopy," J. Biomed. Opt. **11**(4), 044005 (2006).

#260927 Received 10 Mar 2016; revised 5 May 2016; accepted 10 May 2016; published 16 May 2016

7. A. Corlu, R. Choe, T. Durduran, M. A. Rosen, M. Schweiger, S. R. Arridge, M. D. Schnall, and A. G. Yodh, "Three-dimensional in vivo fluorescence diffuse optical tomography of breast cancer in humans," Opt. Express **15**(11), 6696–6716 (2007).
8. S. P. Poplack, K. D. Paulsen, A. Hartov, P. M. Meaney, B. W. Pogue, T. D. Tosteson, M. R. Grove, S. K. Soho, and W. A. Wells, "Electromagnetic breast imaging: average tissue property values in women with negative clinical findings," Radiology **231**(2), 571–580 (2004).
9. S. Jiang, B. W. Pogue, C. M. Carpenter, S. P. Poplack, W. A. Wells, C. A. Kogel, J. A. Forero, L. S. Muffly, G. N. Schwartz, K. D. Paulsen, and P. A. Kaufman, "Evaluation of breast tumor response to neoadjuvant chemotherapy with tomographic diffuse optical spectroscopy: case studies of tumor region-of-interest changes," Radiology **252**(2), 551–560 (2009).
10. M. Bartek, X. Wang, W. Wells, K. D. Paulsen, and B. W. Pogue, "Estimation of subcellular particle size histograms with electron microscopy for prediction of optical scattering in breast tissue," J. Biomed. Opt. **11**(6), 064007 (2006).
11. X. Wang, B. W. Pogue, S. Jiang, H. Dehghani, X. Song, S. Srinivasan, B. A. Brooksby, K. D. Paulsen, C. Kogel, S. P. Poplack, and W. A. Wells, "Image reconstruction of effective Mie scattering parameters of breast tissue in vivo with near-infrared tomography," J. Biomed. Opt. **11**(4), 041106 (2006).
12. N. Shah, A. Cerussi, C. Eker, J. Espinoza, J. Butler, J. Fishkin, R. Hornung, and B. Tromberg, "Noninvasive functional optical spectroscopy of human breast tissue," Proc. Natl. Acad. Sci. U.S.A. **98**(8), 4420–4425 (2001).
13. S. Srinivasan, B. W. Pogue, S. Jiang, H. Dehghani, C. Kogel, S. Soho, J. J. Gibson, T. D. Tosteson, S. P. Poplack, and K. D. Paulsen, "Interpreting hemoglobin and water concentration, oxygen saturation, and scattering measured in vivo by near-infrared breast tomography," Proc. Natl. Acad. Sci. U.S.A. **100**(21), 12349–12354 (2003).
14. B. J. Tromberg, N. Shah, R. Lanning, A. Cerussi, J. Espinoza, T. Pham, L. Svaasand, and J. Butler, "Non-invasive in vivo characterization of breast tumors using photon migration spectroscopy," Neoplasia **2**(1-2), 26–40 (2000).
15. P. Taroni, G. Danesini, A. Torricelli, A. Pifferi, L. Spinelli, and R. Cubeddu, "Clinical trial of time-resolved scanning optical mammography at 4 wavelengths between 683 and 975 nm," J. Biomed. Opt. **9**(3), 464–473 (2004).
16. B. W. Pogue, S. P. Poplack, T. O. McBride, W. A. Wells, K. S. Osterman, U. L. Osterberg, and K. D. Paulsen, "Quantitative hemoglobin tomography with diffuse near-infrared spectroscopy: pilot results in the breast," Radiology **218**(1), 261–266 (2001).
17. V. Ntziachristos, A. G. Yodh, M. D. Schnall, and B. Chance, "MRI-guided diffuse optical spectroscopy of malignant and benign breast lesions," Neoplasia **4**(4), 347–354 (2002).
18. A. Cerussi, D. Hsiang, N. Shah, R. Mehta, A. Durkin, J. Butler, and B. J. Tromberg, "Predicting response to breast cancer neoadjuvant chemotherapy using diffuse optical spectroscopy," Proc. Natl. Acad. Sci. U.S.A. **104**(10), 4014–4019 (2007).
19. C. Zhou, R. Choe, N. Shah, T. Durduran, G. Yu, A. Durkin, D. Hsiang, R. Mehta, J. Butler, A. Cerussi, B. J. Tromberg, and A. G. Yodh, "Diffuse optical monitoring of blood flow and oxygenation in human breast cancer during early stages of neoadjuvant chemotherapy," J. Biomed. Opt. **12**(5), 051903 (2007).
20. Q. Zhu, P. A. DeFusco, A. Ricci, Jr., E. B. Cronin, P. U. Hegde, M. Kane, B. Tavakoli, Y. Xu, J. Hart, and S. H. Tannenbaum, "Breast cancer: assessing response to neoadjuvant chemotherapy by using US-guided near-infrared tomography," Radiology **266**(2), 433–442 (2013).
21. H. Soliman, A. Gunasekara, M. Rycroft, J. Zubovits, R. Dent, J. Spayne, M. J. Yaffe, and G. J. Czarnota, "Functional imaging using diffuse optical spectroscopy of neoadjuvant chemotherapy response in women with locally advanced breast cancer," Clin. Cancer Res. **16**(9), 2605–2614 (2010).
22. D. Roblyer, S. Ueda, A. Cerussi, W. Tanamai, A. Durkin, R. Mehta, D. Hsiang, J. A. Butler, C. McLaren, W.-P. Chen, and B. Tromberg, "Optical imaging of breast cancer oxyhemoglobin flare correlates with neoadjuvant chemotherapy response one day after starting treatment," Proc. Natl. Acad. Sci. U.S.A. **108**(35), 14626–14631 (2011).
23. R. Choe, A. Corlu, K. Lee, T. Durduran, S. D. Konecky, M. Grosicka-Koptyra, S. R. Arridge, B. J. Czerniecki, D. L. Fraker, A. DeMichele, B. Chance, M. A. Rosen, and A. G. Yodh, "Diffuse optical tomography of breast cancer during neoadjuvant chemotherapy: a case study with comparison to MRI," Med. Phys. **32**(4), 1128–1139 (2005).
24. S. Jiang, B. W. Pogue, P. A. Kaufman, J. Gui, M. Jermyn, T. E. Frazee, S. P. Poplack, R. DiFlorio-Alexander, W. A. Wells, and K. D. Paulsen, "Predicting breast tumor response to neoadjuvant chemotherapy with diffuse optical spectroscopic tomography prior to treatment," Clin. Cancer Res. **20**(23), 6006–6015 (2014).
25. H. M. Kuerer, A. A. Sahin, K. K. Hunt, L. A. Newman, T. M. Breslin, F. C. Ames, M. I. Ross, A. U. Buzdar, G. N. Hortobagyi, and S. E. Singletary, "Incidence and impact of documented eradication of breast cancer axillary lymph node metastases before surgery in patients treated with neoadjuvant chemotherapy," Ann. Surg. **230**(1), 72–78 (1999).
26. H. M. Kuerer, L. A. Newman, T. L. Smith, F. C. Ames, K. K. Hunt, K. Dhingra, R. L. Theriault, G. Singh, S. M. Binkley, N. Sneige, T. A. Buchholz, M. I. Ross, M. D. McNeese, A. U. Buzdar, G. N. Hortobagyi, and S. E. Singletary, "Clinical course of breast cancer patients with complete pathologic primary tumor and axillary lymph node response to doxorubicin-based neoadjuvant chemotherapy," J. Clin. Oncol. **17**(2), 460–469 (1999).

#260927 Received 10 Mar 2016; revised 5 May 2016; accepted 10 May 2016; published 16 May 2016

27. R. A. De Blasi, S. Fantini, M. A. Franceschini, M. Ferrari, and E. Gratton, "Cerebral and muscle oxygen saturation measurement by frequency-domain near-infra-red spectrometer," Med. Biol. Eng. Comput. **33**(2), 228–230 (1995).
28. T. J. Farrell, M. S. Patterson, and B. Wilson, "A diffusion theory model of spatially resolved, steady-state diffuse reflectance for the noninvasive determination of tissue optical properties in vivo," Med. Phys. **19**(4), 879–888 (1992).
29. C. D'Andrea, L. Spinelli, A. Bassi, A. Giusto, D. Contini, J. Swartling, A. Torricelli, and R. Cubeddu, "Time-resolved spectrally constrained method for the quantification of chromophore concentrations and scattering parameters in diffusing media," Opt. Express **14**(5), 1888–1898 (2006).
30. P. Taroni, D. Comelli, A. Pifferi, A. Torricelli, and R. Cubeddu, "Absorption of collagen: effects on the estimate of breast composition and related diagnostic implications," J. Biomed. Opt. **12**(1), 014021 (2007).
31. Y. Zhao, M. A. Mastanduno, S. Jiang, F. El-Ghussein, J. Xu, J. Gui, B. W. Pogue, and K. D. Paulsen, "Systematic optimization of MRI guided near infrared diffuse optical spectroscopy in breast," in *SPIE BiOS*(International Society for Optics and Photonics2015), pp. 931605–931605–931608.
32. Y. Zhao, M. A. Mastanduno, S. Jiang, F. Ei-Ghussein, J. Gui, B. W. Pogue, and K. D. Paulsen, "Optimization of image reconstruction for magnetic resonance imaging-guided near-infrared diffuse optical spectroscopy in breast," J. Biomed. Opt. **20**(5), 056009 (2015).
33. J. Wang, S. Jiang, Z. Li, R. M. diFlorio-Alexander, R. J. Barth, P. A. Kaufman, B. W. Pogue, and K. D. Paulsen, "In vivo quantitative imaging of normal and cancerous breast tissue using broadband diffuse optical tomography," Med. Phys. **37**(7), 3715–3724 (2010).
34. F. El-Ghussein, M. A. Mastanduno, S. Jiang, B. W. Pogue, and K. D. Paulsen, "Hybrid photomultiplier tube and photodiode parallel detection array for wideband optical spectroscopy of the breast guided by magnetic resonance imaging," J. Biomed. Opt. **19**(1), 011010 (2013).
35. S. Jiang, B. W. Pogue, A. M. Laughney, C. A. Kogel, and K. D. Paulsen, "Measurement of pressure-displacement kinetics of hemoglobin in normal breast tissue with near-infrared spectral imaging," Appl. Opt. **48**(10), D130–D136 (2009).
36. M. A. Mastanduno, S. Jiang, R. Diflorio-Alexander, B. W. Pogue, and K. D. Paulsen, "Automatic and robust calibration of optical detector arrays for biomedical diffuse optical spectroscopy," Biomed. Opt. Express **3**(10), 2339–2352 (2012).
37. H. Dehghani, M. E. Eames, P. K. Yalavarthy, S. C. Davis, S. Srinivasan, C. M. Carpenter, B. W. Pogue, and K. D. Paulsen, "Near infrared optical tomography using NIRFAST: Algorithm for numerical model and image reconstruction," Commun. Numer. Methods Eng. **25**(6), 711–732 (2009).
38. M. A. Mastanduno, J. Xu, F. El-Ghussein, S. Jiang, H. Yin, Y. Zhao, K. Wang, F. Ren, J. Gui, B. W. Pogue, and K. D. Paulsen, "MR-Guided Near-Infrared Spectral Tomography Increases Diagnostic Performance of Breast MRI," Clin. Cancer Res. **21**(17), 3906–3912 (2015).
39. N. Shah, A. E. Cerussi, D. Jakubowski, D. Hsiang, J. Butler, and B. J. Tromberg, "Spatial variations in optical and physiological properties of healthy breast tissue," J. Biomed. Opt. **9**(3), 534–540 (2004).
40. D. R. Leff, O. J. Warren, L. C. Enfield, A. Gibson, T. Athanasiou, D. K. Patten, J. Hebden, G. Z. Yang, and A. Darzi, "Diffuse optical imaging of the healthy and diseased breast: a systematic review," Breast Cancer Res. Treat. **108**(1), 9–22 (2008).
41. L. Spinelli, A. Torricelli, A. Pifferi, P. Taroni, G. M. Danesini, and R. Cubeddu, "Bulk optical properties and tissue components in the female breast from multiwavelength time-resolved optical mammography," J. Biomed. Opt. **9**(6), 1137–1142 (2004).
42. X. Gu, Q. Zhang, M. Bartlett, L. Schutz, L. L. Fajardo, and H. Jiang, "Differentiation of cysts from solid tumors in the breast with diffuse optical tomography," Acad. Radiol. **11**(1), 53–60 (2004).
43. Q. Zhang, T. J. Brukilacchio, A. Li, J. J. Stott, T. Chaves, E. Hillman, T. Wu, M. Chorlton, E. Rafferty, R. H. Moore, D. B. Kopans, and D. A. Boas, "Coregistered tomographic x-ray and optical breast imaging: initial results," J. Biomed. Opt. **10**(2), 024033 (2005).
44. M. A. Mastanduno, J. Xu, F. El-Ghussein, S. Jiang, H. Yin, Y. Zhao, K. E. Michaelsen, K. Wang, F. Ren, B. W. Pogue, and K. D. Paulsen, "Sensitivity of MRI-guided near-infrared spectroscopy clinical breast exam data and its impact on diagnostic performance," Biomed. Opt. Express **5**(9), 3103–3115 (2014).
45. A. M. Shannon, D. J. Bouchier-Hayes, C. M. Condron, and D. Toomey, "Tumour hypoxia, chemotherapeutic resistance and hypoxia-related therapies," Cancer Treat. Rev. **29**(4), 297–307 (2003).

1. Introduction

Breast cancer is a complex disease that presents challenges for both detection and treatment. Neoadjuvant chemotherapy (NAC) is used to treat patients with locally advanced cancers [1]. Accurate imaging can play an important role in patient management. Ultrasonography and mammography are only moderately helpful in monitoring NAC [2]. Dynamic contrast-enhanced magnetic resonance imaging (MRI) and Fluorine 18 fluorodeoxyglucose positron emission tomography (PET) are more successful and have been used by several groups to quantify changes in breast tumors during treatment [3–5]. However, both MRI and PET

#260927 Received 10 Mar 2016; revised 5 May 2016; accepted 10 May 2016; published 16 May 2016

require injection of contrast agents, and the cost of these procedures can be prohibitive. Near infrared spectroscopy and spectral tomography (NIRST) are emerging functional techniques, which estimate the intrinsic biophysical composition of tissue, in terms of concentrations of total hemoglobin and oxy-hemoglobin, water and lipids [6–9]. In addition, the ultra-structural cellular density and size ensemble associated with the extracellular matrix and subcellular constituents of breast tissue can be interrogated through the NIRST scattering spectrum [10, 11]. NIRST offers potential advantages over other imaging candidates because of its noninvasive nature, relatively low cost and portable size, which makes possible repeated imaging procedures under various patient conditions. In this study, a mobile system design is presented which images the breast with 9 wavelengths in a few minutes allowing the unit to be used in a clinical oncology infusion suite.

NIRST has measured the physiological differences in healthy breast tissues [12–15], and detected lesions with high optical contrast [16, 17]. Pilot studies have shown that NIRST monitors tumor response during treatment and can yield prognostic information [9, 18–23]. In a previous study [24], breast cancer patients undergoing NAC were imaged with NIRST before, during and after treatment. Significant differences were found between pathologic complete response (pCR) and pathologic incomplete response (pIR) groups, based on the relative change in tumor HbT within the first cycle of treatment. Moreover, pretreatment HbT relative to the contralateral breast showed potential to separate pCR from pIR. Since pCR patients have been reported to experience higher disease-free survival rates [25, 26], monitoring and early prediction of pCR/pIR category has potential to individualize patient treatment plans even before the therapy begins. Imaging costs and exam time are barriers to clinical adoption. Thus, a major goal of this work was to develop a system which functions in the chemotherapy infusion suite, efficiently and effectively.

NIRST systems typically have source-detector schemes that incorporate either frequency-domain (FD) [27], continuous-wave (CW) [28], or time-domain (TD) [29, 30] data acquisition. FD measurements using intensity-modulated sources are stable and cost effective, but have limited wavelength range because the response of photomultiplier (PMT) detectors drops dramatically above 825nm. As a result, accurate recovery of water and lipid content is limited with FD data alone because these chromophores have characteristic absorption peaks at 975nm and 930nm, respectively. In recent near-infrared enhanced APDs such as S11519 series from Hamamatsu, MEMS technology is utilized to enhance the sensitivity in the near IR region, extending the spectral response range to 600-1150nm. However, the relatively limited gain for the APDs from 10^1 to 10^3 gives much narrower dynamic range than the PMTs used in the current system (10^5). CW systems usually cover a much broader wavelength range, but do not provide patient-specific scatter information. Scattering amplitude and scattering power are important for accurate recovery of other absorption derived optical parameters, especially in the case of NIRST without guidance on tumor position from other imaging modalities [31]. Further, scatter components, themselves, are potential biomarkers for differentiating breast abnormalities and predicting tumor responses to treatment [32]. FD + CW NIRST systems [33, 34], which acquire both FD and CW data, achieve spatial reconstruction of oxy- and deoxy-hemoglobin, water and lipid, as well as scattering amplitude and scattering power. Sequential measurement of multiple wavelengths is time consuming; hence, simultaneous acquisition of multiple wavelengths is attractive [35], and is developed here in tomographic mode.

Based on an existing NIRST approach [34], a portable 9-wavelength FD + CW system was developed. The acquisition time was reduced substantially through simultaneous acquisition of multiple FD and CW channels. A supine optical interface was designed to accommodate different breast shapes and sizes. The performance of the system was validated in phantom, normal subject and cancer patient measurements. The system provides tomographically reconstructed images of the breast that can be used to monitor tumor response to neoadjuvant therapy dynamically.

#260927 Received 10 Mar 2016; revised 5 May 2016; accepted 10 May 2016; published 16 May 2016

2. Methods and materials

2.1 Imaging system

The FD + CW NIRST system was modified based on an existing design developed by El-Ghussein *et al* [34]. The photomultiplier (PMT)/photodiode (PD) detection module enabled both FD and CW acquisition. However, the previous design performed sequential measurements, one wavelength at one time, which required up to 20 minutes to complete. To reduce exam time through simultaneous wavelength acquisition, a three-wavelength FD source module and a six-wavelength CW source module were developed. Sixteen customized 3-meter long bifurcated fiber bundles were introduced as well.

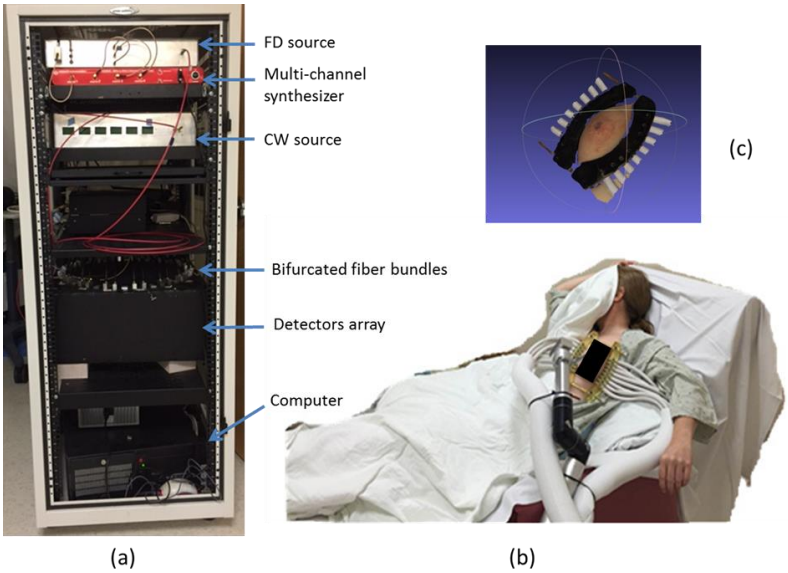

Fig. 1. FD + CW NIRST system. (a) The mobile unit with dimensions of 160cm × 63cm × 85cm. (b) Subject being imaged with the system. (c) Surface image of breast-interface.

Figure 1(a) shows the system configuration with its main components housed in a portable cart. The FD source module consists of three laser diodes (661nm, 785nm and 826nm), modulated by high frequency (~100MHz) signals generated from a multi-channel RF synthesizer (HS2004, Holzworth Instruments). The CW source module consists of six laser diodes (850nm, 905nm, 915nm, 940nm, 975nm and 1064nm), and is modulated by low frequency sinusoidal signals generated directly from the data acquisition board (USB 6255, National Instruments). A three-to-one fiber combiner couples the light from three FD laser diodes into a single FD source fiber. Similarly, a six-to-one fiber combiner couples the light from six CW laser diodes into a single CW source fiber.

A custom programmable mechanical rotary switch connects PMT (H9305-3, Hamamatsu, Japan) and PD (C10439-03, Hamamatsu, Japan) detectors for FD and CW measurement, respectively. Fifteen pairs of PMT and PD detectors and one pair of alignment lens are mounted evenly on the top plate of the rotary stage. The details of the rotary could referred to reference [34]. Two optical fibers with diameter of 800 μm deliver light from the FD and CW source modules into the pair of alignment lens, respectively. The two ends of each of the sixteen bifurcated optical fiber bundles are mounted on another plate, which is fixed separately on top of the rotating circular plate. The circular plate housing the PMT/PD detectors is controlled by a programmable motor to enable source-detector multiplexing. The pair of alignment lens is connected to the two ends of one bifurcated fiber, while the other 15 pairs of PMT and PD detectors are aligned with the two ends of the other 15 bifurcated fiber

#260927 Received 10 Mar 2016; revised 5 May 2016; accepted 10 May 2016; published 16 May 2016

bundles. The single ends of 16 bifurcated fiber bundles are attached to a fiber-breast interface, to deliver source and collect transmittance light (Fig. 1(c)). The rotary switch is incremented 15 times to complete the measurements, yielding a total of 240 (16 × 15) source-detector combinations. The bifurcated fiber bundles allow the simultaneous acquisition of both FD and CW data.

As shown in Fig. 1(b), sixteen bifurcated fiber bundles are grouped into two plastic tubes, which are held by an adjustable arm with three degrees of freedom. The single end of two groups of bifurcated fiber bundles are attached to the breast through an adjustable interface designed to fit various breast shapes and sizes. During optical measurement, the patient sits in a chair, with one side of the breast connected to the imaging system through the fiber-breast interface (Fig. 1(c)). A black sheet covers the patient to prevent room light from interfering with the data acquisition. The optical measurements are easily completed in the infusion room given the positioning flexibility of this portable NIRST system.

2.2 Simultaneous acquisition at multiple wavelengths

Figure 2 shows a system diagram for simultaneous acquisition of both FD and CW measurements. The data flow of the high frequency (~100 MHz) and low frequency (<150Hz) electrical signals, and light are represented by blue, black and red solid lines, respectively. Three channels from the multi-channel synthesizer provide three RF signals with the same power of 13dBm but at slightly different frequencies of F1 = 100.0004MHz, F2 = 100.0007MHz, and F3 = 100.0011MHz, respectively. Another channel provides a reference signal modulated at 100MHz for phase-locked detection. The three RF signals are combined with three DC current lines through bias-tees to drive three laser diodes (LD1 = 661nm, LD2 = 785nm, and LD3 = 826nm, respectively). Six low-frequency sinusoidal signals (F4 – F9) are generated from the DAQ board, to drive six laser diodes at 850nm, 905nm, 915nm, 940nm, 975nm, and 1064nm, respectively. Custom fiber combiners connect the 3 FD and 6 CW lasers. Although the hardware is capable of delivering and collecting all nine channels of light at the same time, best practice divides the nine channels into two sets, mixing signals which are maximally separated but can be measured simultaneously. The total power of any six sources used at one time is less than 120mW, and the cross-talk is less than 0.8% between different channels. The modulation frequencies of the six CW channels are set to 50Hz, 90Hz and 110Hz for LD4/LD7, LD5/LD8, and LD6/LD9, respectively.

#260927 Received 10 Mar 2016; revised 5 May 2016; accepted 10 May 2016; published 16 May 2016

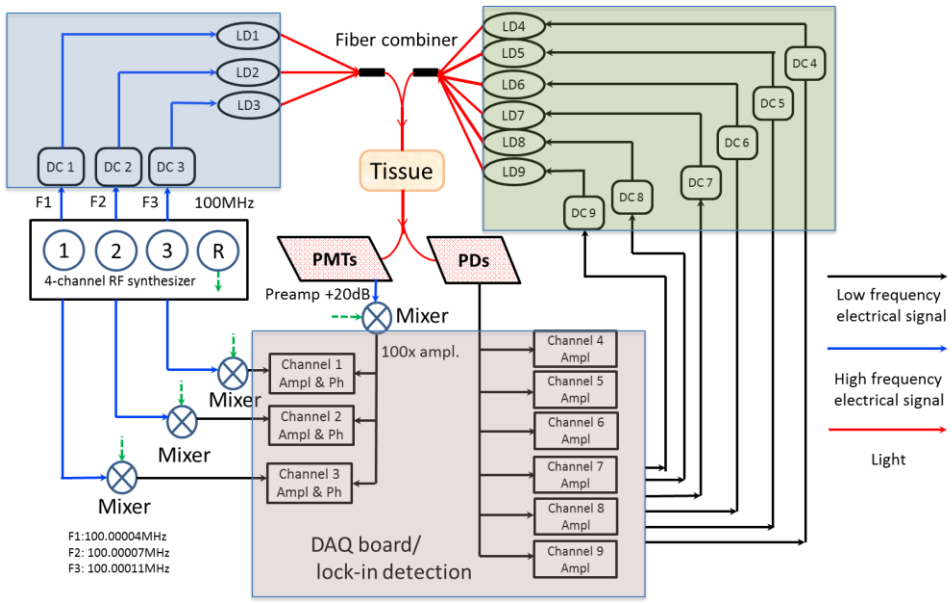

Fig. 2. System diagram for simultaneous acquisition. FD source module, CW source module, and data acquisition/processing module are highlighted in blue, green, and violet blocks, respectively. The flow of low frequency electrical signal, high frequency electrical signal, and light is shown by the black, blue and red solid lines, respectively.

The combined FD and CW light is coupled into two ends of one bifurcated fiber bundle, whose distal end delivers the illumination consisting of six wavelengths modulated at six different frequencies to the breast surface. The transmittance light is collected by the single end of the other fifteen fiber bundles. For each of the fifteen bifurcated fiber bundles, the transmittance light is delivered to pairs of PMT and PD detectors. To ensure the PDs do not saturate in the presence of high frequency modulated signals at shorter wavelengths, thin film long pass filters (87C, Kodak) were installed on the detector windows to block light shorter than 850nm. The RF output from the PMT detectors is amplified by a 20dB low-noise preamplifier, which also filters out residual DC components. The output of the preamplifier is heterodyned with a 100MHz reference signal through a mixer, down-converting it to the lower frequencies 400Hz, 700Hz and 1100Hz. These low frequency signals are amplified (100X) and filtered again to reduce high frequency noise. The resulting signal is read and processed by a DAQ board (USB 6255, National Instruments), where the phase shift and amplitude are extracted for the three shorter wavelengths. Since the phase shift data also depends on the initial phase of each RF output signal from the synthesizer, these signals are passed through RF splitters, and heterodyned with the 100MHz reference signal, to get the initial phase shifts of three components, respectively, which are subtracted in the 3 FD channels. Unlike the FD module, the output of each PD detector is directly connected to the DAQ board. Only the change in amplitude of light propagating through the scattering medium is extracted at the three modulation frequencies. The complete measurement data set consists of amplitude and phase at three shorter wavelengths (661nm, 785nm, and 826nm), and amplitude at six longer wavelengths (850nm, 905nm, 915nm, 940nm, 975nm and 1064nm), for 240 source-detector combinations.

A systematic calibration of the PMT/PD detectors was completed in order to standardize the inter-detector data. In addition to differences in detector responses, other factors, such as fiber loses and rotary switch coupling errors, are corrected during the calibration procedure. Using a central source location relative to all detector fibers, the amplitude/phase response of each PMT detector was characterized for every source position [36]. Sixteen optical fibers

#260927 Received 10 Mar 2016; revised 5 May 2016; accepted 10 May 2016; published 16 May 2016

were placed evenly around a homogeneous circular breast tissue simulating phantom, and a fiber with core diameter of 800μm, delivered source light into the phantom from the top center. The power of source light was attenuated systematically in order to obtain the amplitude/phase response to the light over the dynamic range of 10pW to 1μW. The same procedure was repeated for all possible combinations of wavelengths, PMT gain settings, and modulation frequencies. Similarly, the amplitude response of each PD detector was characterized for every source position, for six wavelengths at corresponding modulation frequencies. After calibration, changes in amplitude and phase shift for a given source-detector pair arise largely from photon absorption and scattering in the breast tissue, which allows accurate reconstruction of desired optical properties.

2.3 Comparison between sequential and simultaneous measurement

PMT detectors at different positions, relative to the source, receive levels of light which could be different by orders of magnitude. In order to account for the variability, corresponding gains are set for 240 source-detector pairs via a dynamic automated gain adjustment algorithm where the PMT gain (control adjustable 0 – 1.1 V) of each source-detector pair increased from 0.4 V (in increments of 0.1V) until the AC component of the amplified output signal reached at least 0.01V, or the highest possible gain setting was reached. The dynamic adjustment ensures that the input light intensity falls in the optimal linear response range. During simultaneous measurements involving 3 frequency (wavelength) signals, the dynamic gain adjustment algorithm applied gains based on the AC signal of the 785nm (700Hz) component.

Compared to the sequential measurements recorded by our previous system [34], the new unit is much faster. Previously, a complete set of sequential measurements involving six wavelengths required 12min, whereas the new simultaneous measurement scheme only requires about 90 seconds, which is sufficient for monitoring of patient response during neoadjuvant chemotherapy with adequate temporal resolution, since a typical infusion procedure takes 2-3 hours. Moreover, reduced acquisition time encourages more patients to participate in the clinical study.

A silicone phantom was used to compare amplitude/phase data obtained with simultaneous versus sequential acquisition. The average relative differences between the two measurement methods in amplitude and phase was 0.8% for intensity and 0.6 degrees in phase, for the 661nm channel, 1.0% and 0.8 degree for the 785nm channel, and 1.1% and 0.9 degree for 826nm channel, respectively. Relative differences were found to be 0.6%, 0.5%, 0.7%, 0.6%, 0.8%, and 1.0% for the CW wavelength channels of 850nm, 905nm, 915nm, 940nm, 975nm, and 1064nm, respectively. These results demonstrate the data quality of simultaneous recording is essentially equivalent to sequential acquisition.

In order to validate the system stability and reproducibility, repetitive measurements were completed on a circular silicone phantom with the diameter of 86mm. The phantom experiment was run 10 times over the short term (15mins), 30 times over the medium term (90mins), and 50 times over the long term (2 weeks when the system was power cycled). Mean value of recovered absorption and scattering coefficient, and relative standard deviation (divided by the mean) were calculated. It was found that the mean value of μa and μ's was $0.0044mm^{-1}$ and $1.2mm^{-1}$, respectively. The relative standard deviation of μa & μ's was 0.55% & 0.67%, 1.05% & 0.98%, and 1.50% & 1.10% over short, medium and long terms, respectively. Such variation might come from thermal shift of system components such as lasers and PMT/PD detectors. Phase/frequency shift from multi-channel synthesizer could contribute to the system errors as well.

2.4 Breast interface

In this study, a parallel optical interface was incorporated with an articulating arm to provide robust optical measurements within a flexible patient setup. The interface consisted of

#260927 Received 10 Mar 2016; revised 5 May 2016; accepted 10 May 2016; published 16 May 2016

opposing plates with a slight curvature, designed using Solidworks and fabricated with a three-dimensional printer (Stratasys, Inc., Eden Prairie, MN). The interface was blackened on its exterior to dampen stray illumination from light reflections. The sixteen optics fiber bundles were divided into two sets of eight, placed in the same plane, and connected through two slim rods that allowed adjustments to fit specific breast sizes. During a breast exam, the interface was opened to its maximum extent and then closed, until all (most) fibers achieved good contact with breast tissue by applying a modest amount of pressure. The weight of the interface and fiber bundles was held in place by the articulating arm which was placed close to the breast. The clinical exam attendant positioned the optical interface measurement plane across the tumor based on prior information from mammography/MRI images. The position and orientation of the breast interface was also adjusted to maximize intersection with the tumor, by imaging in one of the mediolateral (ML), mediolateral oblique (MLO) or craniocaudal (CC) geometries commonly used in mammography. Setup of the breast interface required 2~3 mins and most participants did not indicate feelings of discomfort. After the interface was setup, the fibers which did not have good contact with the breast were noted. The corresponding boundary data was eliminated from the data set for future image reconstruction. Separation between the two breast interface sections was measured and used to make patient specific 2D FEM models. Two breast interfaces with different curvatures were designed to accommodate various breast sizes and tumor locations. Their performances are compared in Section 3.

2.5 Image reconstruction

An open source software platform, NIRFAST [37], was used to process and calibrate boundary amplitude and phase data, make patient specific 2D FEM meshes, and reconstruct optical NIRST images. In this approach, the propagation of photons is approximated by the diffusion equation. Calculation of the diffusion model follows from the frequency domain equation:

$$-\nabla\cdot\mathbf{D}(\mathbf{r})\nabla\Phi(\mathbf{r},\omega)+\left(\mu_a(\mathbf{r})+i\omega/c\right)\Phi(\mathbf{r},\omega)=Q_o(\mathbf{r},\omega) \tag{1}$$

discretized on finite elements. Here, an isotropic source, Q_0, with source frequency, ω, at position, $\mathbf{r}$, delivers light through turbid media. Φ represents the fluence rate at position $\mathbf{r}$, and $\mathbf{D}(\mathbf{r})$ is the optical diffusion coefficient. The fluence rate is calculated using the optical properties, iteratively estimated from the inverse model, and the difference between measured and computed model values of light propagation through the medium is minimized during recovery of the desired optical properties.

The optical properties are estimated during the inverse model solution, using a modified-Tikhonov minimization, which is often applied to stabilize ill-conditioned linear systems of equations. A Newton-type Levenberg-Marquardt (LM) procedure is utilized to obtain the iterative update equation:

$$\left(J^TJ+\bar{\lambda}I\right)^{-1}J^T\delta\Phi=\delta\mu \tag{2}$$

where I is the identity matrix and J is the Jacobian matrix, constructed using both amplitude and phase data. Here, λ is the regularization parameter which balances the relative magnitudes of the two parts of the objective function consisting of the data-model mismatch and the current difference between the estimate and initial guess of optical properties. The update vector, $\delta\mu=\mu_i-\mu_0$, is obtained based on the data-model mismatch, $\delta\phi$, in each iteration. Note that the ill-conditioned Hessian matrix, J^TJ, is stabilized by adding the regularization term $2*\lambda I$. The choice of λ affects the inversion process, and thus, the reconstruction result, and it was chosen based on inherent system noise. A fixed λ of 0.5 was

#260927 Received 10 Mar 2016; revised 5 May 2016; accepted 10 May 2016; published 16 May 2016

selected for each iteration, and a maximum number of 10 iterations was used to yield optimal reconstruction contrast. Scattering amplitude and power were first obtained from global fitting of bulk estimate using FD data. The fitted scattering parameters were then used to estimate scattering coefficient at each CW wavelength. The initial guess of chromophore concentrations and scatter were obtained after global fitting, which were later used in the inversion. FD and CW data were used simultaneously for reconstruction, and they were combined to create a larger vector of measurements Φ, with the first half being FD and the second half being CW recordings. The Jacobian matrix was formulated accordingly. Eventually, 2D spatial images of absorption related chromophore concentrations of oxy and deoxy-hemoglobin, water, and lipid content, and scattering related parameters including scattering amplitude (SA) and scattering power (SP) were reconstructed. From the recovered chromophore concentrations, physiologically relevant parameters were also calculated, including total hemoglobin HbT = HbO + Hb, and oxygen saturation StO_2 = HbO/HbT.

The image reconstruction procedure was completed on a 2D FEM mesh. Unlike some other image-guided NIRS systems [20, 38], where 2D/3D meshes are constructed from additional image data obtained with MRI and ultrasound, the portable NIRST system depends on the fiber-breast interface to make case-specific meshes. Two types of meshes were created with surface curvature matching the corresponding interfaces, and the non-contacting area extended to mimic the natural shape of the breast under a modest amount of compression.

2.6 Phantom imaging

Phantom experiments were conducted to validate the performance of the FD + CW NIRST system. Two molds were designed and fabricated through 3D printing, in order to make gelatin phantoms with cross-sections matching the desired shape of breast-mimicking meshes. Phosphate Buffered Saline (PBS), type 1 Agarose (A6013 SIGMA-ALDRICH), 1% Intralipid (20% I.V. Fat Emulsion, Fresenius Kabi), and whole porcine blood were used to provide optical properties similar to normal breast tissue. Homogeneous reference and heterogeneous phantoms with 1-inch diameter inclusions inside were made for both geometries. Both phantoms had background HbT values of 20 uM, and cylindrical inclusions with 1.5X HbT contrast.

2.7 Human subject imaging

All human subject imaging was carried out under a protocol approved by the Committee for the Protection of Human Subjects (CPHS) at Dartmouth-Hitchcock Medical Center. Written consent was obtained for each subject and the nature of procedure was fully explained. The subjects were seated in an adjustable chair in an examination room, and the NIRST system was placed outside. Ten normal subjects were imaged on both the left and right breast. One patient with invasive ductal carcinoma (IDC) was imaged as well. Corresponding ages, breast sizes, mammographic breast densities taken from clinical reports were recorded. A Student's t-test determined whether different breast density groups could be separated given the recovered optical parameters. Significance was achieved at the 95% confidence interval using a two-tailed distribution.

3. Results

3.1 Phantom study

Figure 3 shows phantom experiment setups and reconstructed images of HbT, StO_2, water, lipid, scattering amplitude (SA) and scattering power (SP) for two breast interfaces with different curvatures. The recovered inclusion/background HbT contrasts were 1.40 and 1.38, 6.7% and 8.0% different from the actual contrast of 1.5X, respectively. Both interfaces were able to yield expected background values for StO_2 (>95%), water (>90%) and lipid (<5%), from the spectral coverage provided by the longer wavelengths in the six CW channels.

#260927 Received 10 Mar 2016; revised 5 May 2016; accepted 10 May 2016; published 16 May 2016

Surface artifact, or the unexpected enhancement along the mesh boundary, is a well-known problem in diffuse optical tomography. The flat interface generated more surface artifacts than the first one, which partly accounts for the fact that the flat interface recovered lower contrast. Additionally, the curved interface produced less heterogeneity in the recovered images of chromophore concentrations. In general, the performance of the curved interface with deeper curvature was superior in terms of both reconstruction accuracy and noise level. However, the flat interface was preferred when imaging small breasts because it maintained better fiber-tissue contact under these conditions.

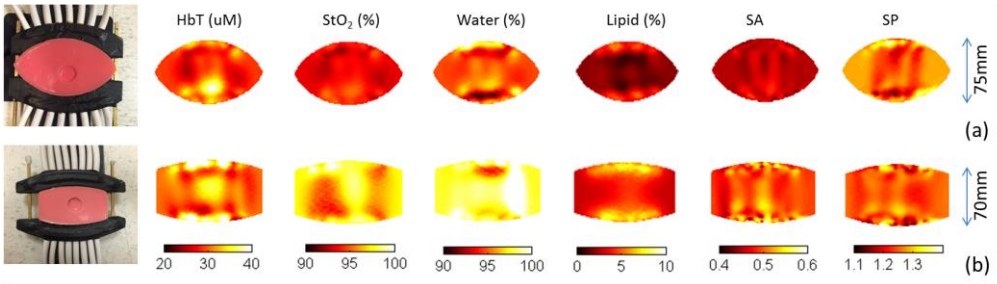

Fig. 3. Experimental setup and reconstructed optical images for two heterogeneous phantoms with 1 inch diameter inclusions. The corresponding interface had deep curvature (a) and flat curvature (b). For both phantoms, the blood concentrations inside and outside the inclusion were 1.5% and 1%, respectively. The interface separation was 75mm and 70mm for the curved and flat interface, respectively.

3.2 Normal subjects study

Both breasts of 10 normal subjects were imaged. Subjects were divided into high and low radiographic density groups based on their recent mammograms. Specifically, fatty and scattered breasts were categorized as low density, and heterogeneously dense (HD) and extremely dense (ED) breasts were considered as high density. Inter-subject and intra-subject variations were also compared with previous studies to validate the performance of the current NIRST system. The temporal variation in optical parameters was investigated as well.

Normalized standard deviation was calculated to evaluate tissue heterogeneity in healthy breast tissue. The spatial variance in HbT, StO2, water and lipid, across the recovered tomographic images of each subject was 13.4%, 7.1%, 14.6% and 13.7%, respectively. The larger variation in the latter two chromophore concentrations arises mainly from the nonuniform distribution of glandular structures in the breast. The low variation in StO_2 agrees with our previous study reported by Wang *et al* [33], and results presented by Shan *et al* [39]. Compared with Wang's data, the results here indicated less variation in water and lipid which may be a consequence of having more CW channels in the longer wavelength range that lead to more accurate reconstruction of water and lipid.

Inter-subject variation for age, body mass index (BMI), HbT, StO_2, water and lipid appears in Table 1. Mean HbT values within the breast ranged from 10.0 to 26.8 μM with an overall subject mean of 18.1 μM. Mean StO_2 within the breast varied from 58.5% to 88.0% with an overall group mean value of 70.5%. The results reported here are consistent with several other studies of asymptomatic breast tissue [38, 40, 41], which also indicate that optical and physiological parameters are significantly affected by biological factors such as age, menopausal status, hormone use, and BMI. Because of the small number of normal subjects evaluated in this study, discussion focuses on the effects of breast density on the recovered optical parameters.

In addition to the inter- and intra-subject variation, differences between left and right sides of the breast were assessed by calculating |left-right|/average*100% for all optical parameters, which were 13.2% for HbT, 5.4% for StO_2, 8.3% for water, and 12.9% for lipid. No

#260927 Received 10 Mar 2016; revised 5 May 2016; accepted 10 May 2016; published 16 May 2016

statistically significant differences were found between the left and right values for breasts imaged.

Table 1. Mean, standard deviation and total range of physiological and optical parameters for 10 normal subjects

Property	Mean Std	Total range
Age, yr.	56.9 ± 6.1	49 – 66
BMI, kg/m^2	28.8 ± 6.8	21.5 – 42.2
HbT, μM	18.1 ± 4.2	10.0 – 26.8
StO_2, %	70.5 ± 8.2	58.5 – 88.0
Water, %	39.4 ± 6.0	32.2 – 52.7
Lipid, %	40.2 ± 15.1	17.2 – 62.2

Since one potentially important feature of the current system is the ability to dynamically monitor patient response during infusion, temporal variation was investigated. Figure 4 shows the recovered optical parameters of two of the ten normal subjects measured continuously for 30 minutes. The standard deviation of 8 continuous acquisitions was calculated and varied for different optical indicators (<5%). Several factors contribute to the temporal variation including breathing pattern and patient movement, and the effects of these variations on the recovery of tumor/background optical contrast needs further investigation.

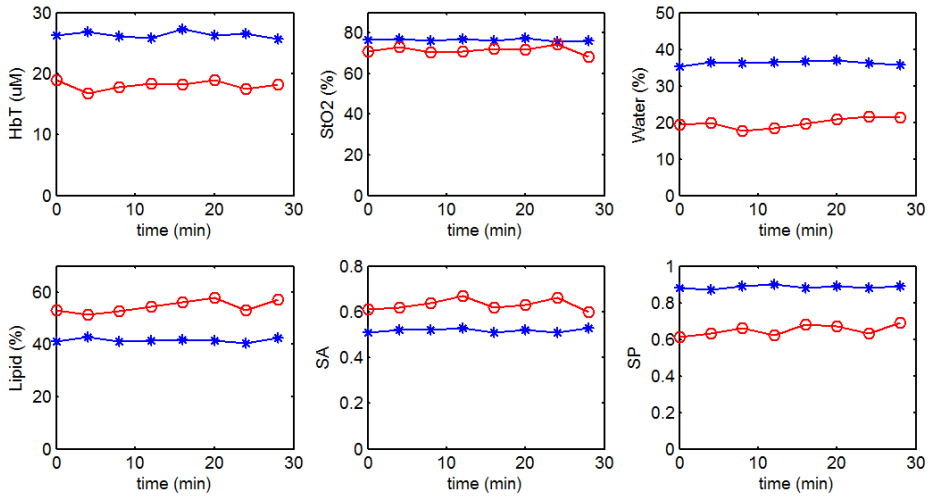

Fig. 4. Continuous measurements of (a) HbT; (b) StO_2; (c) water; (d) lipid; (e) SA and (f) SP for two normal subjects.

Figure 5 shows recovered images of HbT, StO_2, water, lipid, scattering amplitude and scattering power for three normal subjects. The first (Fig. 5(a)) and second (Fig. 5(b)) subject were imaged using the breast interface with a deeper curvature, and had separations between the two fiber holders of 63mm and 85mm, respectively. The third subject had smaller breasts (A cup) and was imaged using the interface with flat curvature and a maximum separation of 40mm. All sixteen fibers contacted the breast well in the three cases. Heterogeneity in the recovered images appears to arise from differences in fibroglandular and adipose content in

#260927 Received 10 Mar 2016; revised 5 May 2016; accepted 10 May 2016; published 16 May 2016

the breast, which varied case by case. No common pattern was found in the recovered images, which suggests that the NIRST system does not introduce systematic bias.

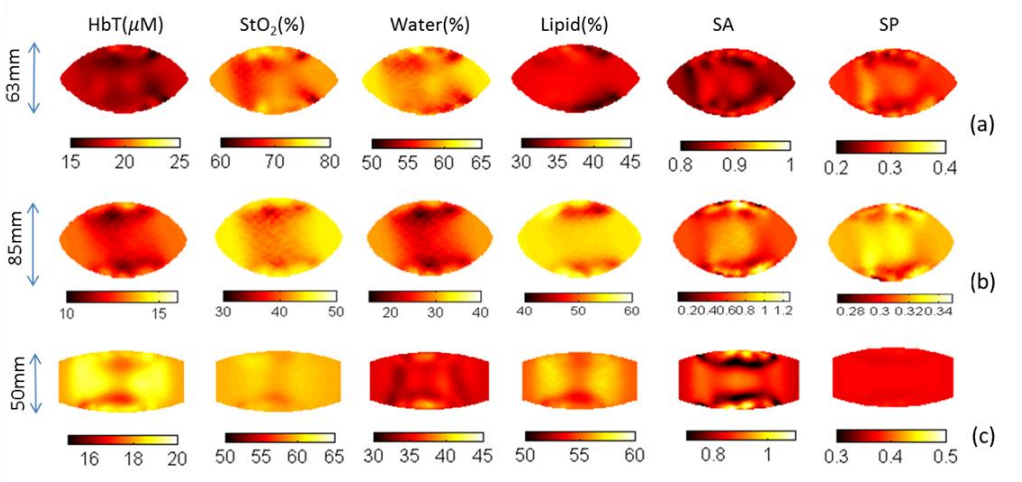

Fig. 5. Recovered optical images of three normal subjects. Maximum separation between the two fiber holders in the interface was 63mm (a), 85mm (b), and 50mm (c), respectively.

Subjects were stratified into high and low density groups based on their mammographic results. Figure 6 shows a comparison, in which significantly ($p<0.05$) higher HbT and water contents were found in the high density group relative to the low density group. No trends in oxygen saturation were identified between the two groups, each being near 70% oxygenated. A strong correlation between NIRST recovered properties and radiographic breast density was observed, as shown previously [13, 14].

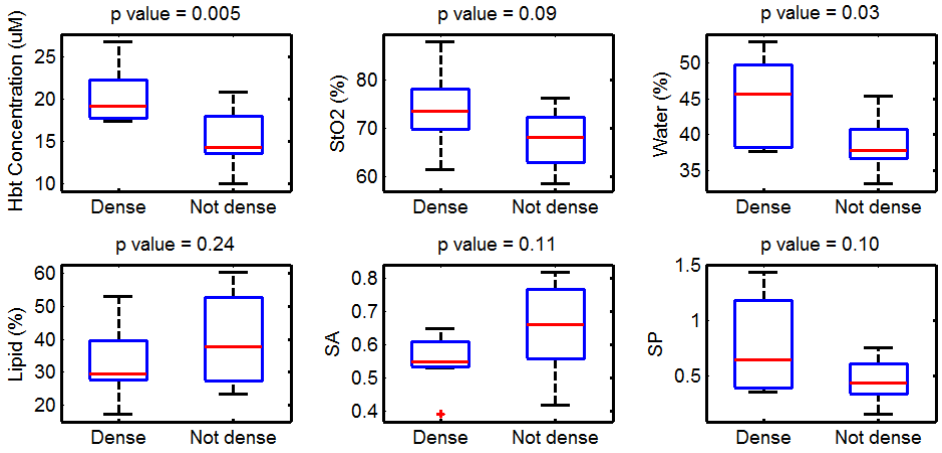

Fig. 6. Data from subjects grouped by mammographic breast density (five subjects per group). HbT: total hemoglobin; StO_2: oxygen saturation; SA: scattering amplitude; SP: scattering power.

3.2 Imaging of breast cancer patient

A 67-year old woman with a 1.1 × 0.9 × 1.2 cm^3 invasive ductal carcinoma in her right breast was imaged on both the left and right breast. The position of the tumor was marked in advance on the breast surface to guide placement of the fiber interface during optical data acquisition. Magnetic resonance (MR) images of the patient were also acquired and displayed in Figs. 7(a)-7(c). Registration between MRI and recovered optical images is difficult to

#260927 Received 10 Mar 2016; revised 5 May 2016; accepted 10 May 2016; published 16 May 2016

accomplish, since the optical interface reshapes the breast relative to MRI. Instead, the end of one fiber, which was positioned on a surface marker placed on the breast during optical measurement, was registered to the position of a skin surface marker in the MRI (seen in the MRI image). Orientation of the breast mesh (1-7 o'clock) was adjusted to coincide with the coordinate system in MRI, as shown in Fig. 7(d). The tumor region was segmented from the recovered HbT image. The average tumor to background contrast was calculated to be 1.41X for HbT, 0.92X for StO_2, 1.23X for water, 0.78X for lipid, 0.95X for scattering amplitude, and 1.08X for scattering power, respectively.

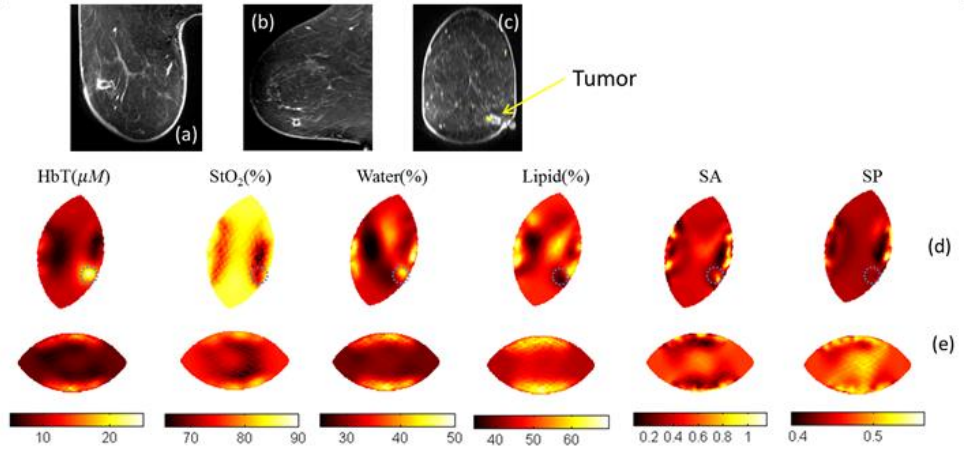

Fig. 7. MRI T2 images of a patient with invasive cancer in the right breast: (a) Axial view, (b) sagittal view and (c) coronal view. Recovered optical images of HbT, StO_2, water, lipid, SA, and SP for right (d) and left (e) breast, respectively. Recovered optical images are displayed in the same orientation in (d) as in (c).

4. Discussion

In this paper, we introduced a portable FD + CW NIRST system with a custom breast interface, and tested its performance on phantoms, normal subjects and a cancer patient. The system was developed based on experience with an existing MR-guided NIRST approach [34], but for the purpose of dynamic monitoring of responses to neoadjuvant chemotherapy within the infusion suite. Studies utilizing diffuse optical tomography technique typically incorporate less than 4 wavelengths in the range of 680 – 850nm [6, 7, 42, 43], which inhibits accurate recovery of water and lipid content. Here, three FD wavelengths and six CW wavelengths provided coverage in the range of 661 – 1064nm. While several studies [20–24] have focused on hemodynamic changes throughout the treatment period, dynamic changes during a single infusion procedure are also of interest. Thus, we adapted the system design to acquire nine FD and CW wavelengths simultaneously, which significantly reduced imaging time. Compared to our previous stand-alone NIRST approach for monitoring patient responses to neoadjuvant chemotherapy, components were integrated into a portable cart. No imaging bed was required, allowing us to acquire data in the clinical infusion suite.

A major improvement in the current system was the breast interface, designed to fit different breast sizes and shapes easily. We have shown that measurement sensitivity, or tumor coverage, plays a critical role in accurate, spatial reconstruction of optical properties [44]. The fiber-breast interface has been investigated extensively for different diffuse optical tomography systems [33, 44]. A common disadvantage of these breast interface geometries was their lack of mobility and the requirement for the patient to be positioned prone on a specific imaging bed during data acquisition. For the purpose of monitoring patient response during neoadjuvant chemotherapy, where the intention is to examine an individual frequently at different time points during treatment, the added convenience is significant. In some cases,

#260927 Received 10 Mar 2016; revised 5 May 2016; accepted 10 May 2016; published 16 May 2016

continuous measurements are desired for dynamic monitoring of response during the infusion procedure. A portable NIRST system with corresponding fiber-breast interface is required to satisfy these conditions.

The FD + CW data acquisition was validated using gelatin phantom experiments with shapes mimicking natural extensions of the breast under modest compression provided by the interface. Two interfaces were evaluated - one with a deeper and one with a flatter surface curvature. For both interfaces, the recovered HbT contrast in the inclusion was found to be slightly lower than the actual value, which is common in diffuse optical tomography [34]. We were able to recover values very close to the actual HbT contrast as well as background values for StO_2, water and lipid using both interfaces. The interface with flatter curvature was used for smaller breasts, and enabled better coupling at all fibers. The other interface with deeper curvature yielded slightly better performance when all fibers were in contact, which was mostly the case for the larger breasts and phantoms considered here.

Relative HbT has been shown to be an indicator of tissue malignancy, widely used to assess changes in tumor physiology during neoadjuvant chemotherapy [22–24]. StO_2 may also be an important index for predicting tumor responses, since hypoxic tumors have been found to be more resistant to chemotherapy [45]. Water, lipid and scatter components have also shown potential to correlate with patient response [18]. As shown in Fig. 4, we were able to image both small and large breasts. The recovered lipid content for the participant imaged with a 63mm interface separation was 35.8%, which was lower than the other two participants. A substantial amount of variation was found in the recovered lipid among 10 normal subjects, with total range from 17.2% to 62.2%, and mean value of 40.2% with standard deviation of 15.1%. The recovered physiologically relevant values of HbT, StO_2, water and lipid all fell into reasonable ranges, and were comparable to previous studies [13–15]. Intra- and inter-subject variations were calculated and compared to our previous work. Temporal variations were also investigated through continuous measurements of 30 minutes. Less than 5% standard deviation in 8 continuous measurements was observed, suggesting the data are stable. No significant difference was found between the two sides of the breast for all optical parameters, which supports use of the average of the contralateral breast imaged before treatment to highlight the tumor/background contrast relative to the surrounding tissue over the course of therapy. Furthermore, these physiological parameters were compared between high and low density groups, and significantly higher HbT and water were found in the high density breasts, consistent with earlier studies [33]. No significant differences were found in the other optical indicators, partly because of the modest sample size in the normal subject groups.

We validated system performance in a patient with subsequently confirmed IDC. The recovered tumor position was in good agreement with that highlighted in MRI. We found significant increases in HbT and water, and decreases in lipid in the tumor region. No significant difference was found in StO_2. These findings are consistent with results for malignant tumors reported in other studies [6, 33].

Although the current system yielded robust measurements with the envisioned ease of use, some challenges remain which need to be addressed carefully. For instance, only 3 wavelength channels are available in the FD mode, which can limit reconstruction accuracy of scatter components. This issue may account for the fact that we did not find significant differences in scattering power between the high and low density groups. Another three-wavelength FD source module could be added into the current 9-wavelength source mode without increasing data acquisition time. Because of the diffusive nature of this tomography approach, further differentiation of adipose and fibroglandular tissue may be challenging without guidance from other imaging modalities, such as MRI or ultrasound. However, the tumor to average background contrast is often the indicator of choice rather than tumor to adipose contrast, or tumor to fibroglandular contrast alone. Although no additional imaging modality was used to guide NIRST during image reconstruction, extra MRI/mammography

#260927 Received 10 Mar 2016; revised 5 May 2016; accepted 10 May 2016; published 16 May 2016

scans were still necessary to indicate the position and orientation of tumor, which was critical for proper placement of the breast interface to ensure tumor coverage.

5. Conclusion

A portable FD + CW NIRST system has been developed for quantifying changes in total hemoglobin, oxygen saturation, water, lipid content, scattering amplitude and scattering power in the breast during neoadjuvant chemotherapy. Simultaneous acquisition of 3 FD wavelength and 6 CW wavelength channels required about 3 minutes. The system was tested on phantoms, healthy subjects and a cancer patient. An adjustable interface was designed to fit different breast shapes and sizes. All components were integrated into a portable system, which allows robust measurements in the infusion unit. An imaging study involving a larger cohort of breast cancer patients receiving clinical oncology treatment is ongoing.

Acknowledgments

This work has been supported by NIH research grant R01 CA176086. We kindly thank Dr. Tom O'Sullivan for his help in making calibration phantom.

#260927 Received 10 Mar 2016; revised 5 May 2016; accepted 10 May 2016; published 16 May 2016